

Intrinsic point defects in aluminum antimonide

Daniel Åberg,* Paul Erhart, Andrew J. Williamson, and Vincenzo Lordi†

Lawrence Livermore National Laboratory, Livermore, California 94551, USA

(Received 16 November 2007; revised manuscript received 7 March 2008; published 25 April 2008)

Calculations within density functional theory on the basis of the local density approximation are carried out to study the properties of intrinsic point defects in aluminum antimonide. Special care is taken to address finite-size effects, band gap error, and symmetry reduction in the defect structures. The correction of the band gap is based on a set of *GW* calculations. The most important defects are identified to be the aluminum interstitial $\text{Al}_{i,\text{Al}}^{1+}$, the antimony antisites Sb_{Al}^0 and $\text{Sb}_{\text{Al}}^{1+}$, and the aluminum vacancy $\text{V}_{\text{Al}}^{3-}$. The intrinsic defect and charge carrier concentrations in the impurity-free material are calculated by self-consistently solving the charge neutrality equation. The impurity-free material is found to be *n*-type conducting at finite temperatures.

DOI: [10.1103/PhysRevB.77.165206](https://doi.org/10.1103/PhysRevB.77.165206)

PACS number(s): 61.72.J-, 61.72.Bb, 61.82.Fk, 71.15.Mb

I. INTRODUCTION

Aluminum antimonide is receiving much renewed interest for applications ranging from ionizing radiation detection to microelectronics and optoelectronics. For gamma radiation detection, AlSb is particularly promising as a novel material that enables high-energy-resolution detection at room temperature due to its indirect band gap of 1.6 eV, the high atomic number of Sb, and the potentially high electron and hole mobilities of up to several hundred $\text{cm}^2 \text{V}^{-1} \text{s}^{-1}$ at room temperature.^{1,2} Improved materials for high resolution, room temperature gamma radiation detectors are critically needed for applications in nuclear nonproliferation and monitoring, homeland security, and also medical and space imaging applications. Such detectors operate by counting the number of electron-hole pairs created in the semiconductor upon interaction with a gamma ray. Thus, a small band gap is generally desired to maximize the number of generated carriers, which increases the signal and reduces the shot noise. However, if the band gap is too small, excess thermal noise is generated from carriers thermally excited across the gap. At room temperature, a gap of ~ 1.6 eV is nearly optimal. In a similar vein, low intrinsic carrier concentrations in the material are desired to reduce the background noise. Furthermore, high energy resolution (adequate counting statistics) is achieved by maximizing the efficiency of charge collection, which requires high carrier mobilities and long carrier lifetimes. An indirect band gap can be advantageous for maximizing carrier lifetimes by quenching radiative recombination. Finally, a high atomic number is desired to increase the stopping power for high energy radiation, which reduces the required size of the device. Presently, the purity of large single-crystal growths of AlSb limits its performance for radiation detection application.

In microelectronics, AlSb and related alloys containing In are finding use in advanced field-effect transistor designs that promise higher switching speeds and lower power consumption as compared to silicon devices.^{3,4} The material has also found use in high current density, high speed resonant tunnel diodes.⁵ In optoelectronics, thin films of AlSb are used in active regions and superlattice structures for claddings in novel type-II infrared cascade lasers.⁶⁻⁸ Such lasers, which emit wavelengths at around 3–4.3 μm , find application in remote atmospheric chemical sensing, for example. Aluminum antimonide is particularly interesting in these applica-

tions because it has a large 2.1 eV conduction band offset with InAs, which often comprises the other key component in the active layers of these devices.

In the present work, we present a careful analysis of the thermodynamic and electronic properties of intrinsic point defects in AlSb, since the electronic and transport properties of the material can be degraded by detrimental defects. The main goals of this study are to identify the most important intrinsic point defects and to establish the concentrations of defects and charge carriers in thermal equilibrium. This work is part of a larger effort to understand the fundamental microscopic limits of performance of this and other semiconductor materials. Future work will focus on extrinsic impurities in the material as well as the implications on carrier transport properties.

Our major findings in this work are that the dominant native defects in AlSb are aluminum interstitials, antimony antisites, and aluminum vacancies, depending on chemical environment and doping. The equilibrium concentration of total native defects near the melting temperature is found to be in the 10^{16} – 10^{17}cm^{-3} range, while at lower temperatures, concentrations down to 10^{10}cm^{-3} or lower are expected. The electron chemical potential in a pure material is near the middle of the band gap; however, the material naturally tends to be slightly *n*-type doped by charged aluminum interstitials.

The paper is organized as follows. In Sec. II, we review the thermodynamic formalism we use to derive defect formation energies and concentrations from first principles calculations, and describe the computational details that underlie the present work. In Sec. III, we report the relaxed defect geometries, defect formation energies, total defect concentrations, and net charge carrier concentrations, which are obtained by self-consistently solving the charge neutrality condition. Finally, in Sec. IV, we discuss the intrinsic limitations of AlSb on the basis of our results and the relation to experimental data. The Appendix contains a brief derivation of the band gap correction scheme utilized in the present work.

II. METHODOLOGY

A. Point defect thermodynamics

A material in thermodynamic equilibrium must contain a certain number of point defects at finite temperature due to

entropy. The temperature dependence of the equilibrium defect concentration can be shown to obey the following relation:⁹

$$c = c_0 \exp\left(-\frac{\Delta G_D}{k_B T}\right), \quad (1)$$

where c_0 denotes the concentration of possible defect sites, k_B is Boltzmann's constant, and T is the absolute temperature. The Gibbs energy of defect formation, ΔG_D , can be split into three distinct terms as follows:

$$\Delta G_D = \Delta E_D + T\Delta S_D + p\Delta V_D. \quad (2)$$

The formation entropy ΔS_D is typically on the order of $1k_B$, so the entropy term hardly exceeds 0.1 eV even at elevated temperatures. In some cases, entropic effects could play a role in stabilizing a defect at high temperatures when the enthalpy differences are small. We do not explicitly treat this effect here, but point out cases in our results where it may be important. The formation volume ΔV_D describes the pressure dependence of the Gibbs energy of formation and is typically some small fraction of the atomic volume, so it can be neglected at ordinary pressures. The most important contribution is the defect formation energy ΔE_D . In the following, we therefore focus on the formation energy and, for simplicity, ignore both the entropy and volume terms.

For a binary compound, the formation energy for a defect in charge state q is given by^{10,11}

$$\begin{aligned} \Delta E_D = E_D - \frac{1}{2}(n_{\text{Al}} + n_{\text{Sb}})\mu_{\text{AlSb}}^{\text{bulk}} - \frac{1}{2}(n_{\text{Al}} - n_{\text{Sb}})(\mu_{\text{Al}}^{\text{bulk}} - \mu_{\text{Sb}}^{\text{bulk}}) \\ - \frac{1}{2}(n_{\text{Al}} - n_{\text{Sb}})\Delta\mu + q(E_{\text{VBM}} + \mu_e), \end{aligned} \quad (3)$$

where E_D is the total energy of the system containing the defect, n_i denotes the number of atoms of type i , μ_i^{bulk} is the chemical potential of component i in its reference state, and we have written the terms using explicit labels for AlSb. By neglecting entropic contributions, the chemical potentials of the reference phases can be replaced by their cohesive energies at 0 K. The formation energy depends on the chemical environment via the parameter $\Delta\mu$, which describes the variation of the chemical potentials under different conditions. The range of $\Delta\mu$ is constrained by the formation energy of AlSb by $|\Delta\mu| \leq \Delta H_f^{\text{AlSb}}$, where for the present convention $\Delta\mu = -\Delta H_f^{\text{AlSb}}$ and $\Delta\mu = +\Delta H_f^{\text{AlSb}}$ correspond to Al- and Sb-rich conditions, respectively. Finally, the formation energy also depends on the electron chemical potential, μ_e , which is measured with respect to the valence band maximum, E_{VBM} .

B. Computational details

The energy terms in Eq. (3) were calculated by using density functional theory (DFT) in the local density approximation (LDA) using the Vienna *Ab initio* simulation package^{12–15} (VASP) and the projector augmented-wave method.^{16,17} Defect formation energies were obtained by using supercells of various sizes containing 32, 64, 128, and

216 atoms. Extrapolation was used to account for finite-size effects as described in detail in Sec. II C. Brillouin zone integrations were performed with k -point grids generated by using the Monkhorst–Pack scheme.¹⁸ For the 32- and 64-atom cells, a nonshifted $6 \times 6 \times 6$ mesh was used, while for the 128-atom cell, a shifted $3 \times 3 \times 3$ grid was used. For the 216-atom cell, a nonshifted $4 \times 4 \times 4$ mesh was constructed. The plane wave cutoff energy was set to 300 eV, and Gaussian smearing with a width of 0.1 eV was used to determine the occupation numbers. For charged defect calculations, a homogeneous background charge was employed (by omitting the $G=0$ term in the potential) to ensure charge neutrality of the entire cell.

Atomic relaxations were performed to determine the equilibrium structures of the defects, with ionic forces converged to 20 meV/Å and all calculations performed at the theoretical equilibrium volume. Relaxations from various randomized initial configurations were performed to avoid high-symmetry local energy minima in the structures.

C. Finite-size corrections

In the supercell approximation, there are spurious interactions between defects and their periodic images, which lead to systematic errors.^{19,20} For neutral defects, the leading error is due to elastic interactions, which cause an overestimation of the formation energy. The strain energy of a pointlike inclusion can be derived from linear elasticity theory and can be shown to fall off roughly with L^{-3} , where L is the distance between periodic images.^{21,22} Therefore, the formation energy in the dilute limit ($L \rightarrow \infty$) can be obtained by finite-size scaling with L^{-3} , which removes the elastic strain component.

Makov and Payne considered the convergence of the energy of charged systems in periodic systems and proposed a correction on the basis of a multipole expansion.²³ The leading term corresponds to the monopole-monopole interaction and scales with L^{-1} . This term can be analytically determined if the static dielectric constant of the medium, ϵ , and the Madelung constant of the Bravais lattice of the supercell, α , are known:^{23,24}

$$\Delta E_{\text{mp}} = -\frac{q^2 \alpha}{2L\epsilon}. \quad (4)$$

The next higher-order term in the expansion is the monopole-quadrupole interaction which scales as L^{-3} . Even higher-order terms [$\mathcal{O}(L^{-n})$, $n \geq 5$] are usually small and, therefore, neglected. In the present work, we have applied the monopole-monopole correction term by using the experimental value for the static dielectric constant ($\epsilon = 12$). Then, since both the elastic and the monopole-quadrupole interactions scale with L^{-3} , we employed finite-size scaling with L^{-3} to correct for these terms. This extrapolation scheme gave very small extrapolation errors as shown in Tables I and II. The results of the finite-size scaling procedure are illustrated in Fig. 1 for the most important defects. Figure 1 clearly illustrates the effect of the monopole-monopole correction term, which tremendously reduces the variation between the supercells. The remaining higher-order variations are very

TABLE I. Formation energies, in eV, of intrinsic point defects under Al-rich ($\Delta\mu=-\Delta H_f$) and Sb-rich ($\Delta\mu=+\Delta H_f$) conditions for an electron chemical potential at the valence band maximum [$\mu_e=0$ eV in Eq. (3)]. Both the as-calculated and the band-gap-corrected formation energies are given. The number of occupied (unoccupied) conduction (valence) band states defined through Eq. (A4) is given in the third column ($\Delta z_{e,h}$), where negative (positive) values correspond to electrons (holes). The extrapolation error, in eV, of the finite-size scaling procedure is given in brackets in the last column.

Defect	q	$\Delta z_{e,h}$	As-calculated		Corrected		
			Al-rich	Sb-rich	Al-rich	Sb-rich	
V_{Sb}	-3		5.42	5.70			(0.04)
	-2		4.48	4.76			(0.04)
	-1	0	3.47	3.75	3.91	4.19	(0.08)
	0		3.29	3.56			(0.07)
	+1	0	2.93	3.21	2.49	2.76	(0.04)
	+2		3.24	3.52			(0.08)
	+3		3.76	4.03			(0.12)
Al_{Sb}	-3		4.72	5.27			(0.05)
	-2	0	3.17	3.72	4.06	4.61	(0.02)
	-1	+1	2.68	3.24	3.57	4.12	(0.01)
	0	+2	2.46	3.01	3.35	3.90	(0.03)
$\text{Al}_{i,\text{Al}}$	-2		5.01	5.29			(0.06)
	-1	-2	3.51	3.78	4.28	4.56	(0.03)
	0	-1	2.22	2.49	2.38	2.66	(0.01)
	+1	0	1.15	1.43	0.71	0.98	(0.01)
	+2	+1	1.44	1.72	1.00	1.27	(0.02)
	+3		1.95	2.22			(0.06)
$\text{Al}_{i,\text{Sb}}$	-2		5.49	5.77			(0.07)
	-1	-2	4.01	4.28	4.78	5.06	(0.03)
	0	-1	2.75	3.03	2.91	3.19	(0.01)
	+1	0	1.73	2.01	1.29	1.56	(0.01)
	+2	+1	1.68	1.96	1.24	1.51	(0.01)
	+3		2.00	2.28			(0.01)
V_{Al}	-3	0	3.99	3.72	5.32	5.04	(0.02)
	-2	+1	3.35	3.07	4.68	4.40	(0.02)
	-1	+2	2.94	2.66	4.27	3.99	(0.03)
	0	+3	2.75	2.47	4.08	3.80	(0.04)
Sb_{Al}	-1		3.25	2.70			(0.03)
	0	0	2.03	1.48	2.03	1.48	(0.02)
	+1	+1	1.52	0.97	1.52	0.97	(0.01)
	+2	+2	1.40	0.85	1.40	0.85	(0.01)
$\text{Sb}_{i,\text{Sb}}$	+2		3.63	3.35			(0.01)
$\text{Sb}_{i,\text{Al}}$	-2		6.32	6.04			(0.10)
	-1	-4	4.84	4.57	5.94	5.66	(0.02)
	0	-3	3.92	3.65	4.41	4.13	(<0.01)
	+1	-2	3.16	2.88	3.04	2.77	(0.13)
	+2	-1	2.93	2.66	2.21	1.93	(0.01)
$\text{Sb}_{i,\text{hex}}$	-2		6.24	5.96			(0.09)
	-1	-4	4.96	4.68	6.06	5.78	(0.02)

TABLE I. (Continued.)

Defect	q	$\Delta z_{e,h}$	As-calculated		Corrected		
			Al-rich	Sb-rich	Al-rich	Sb-rich	
$\text{Sb}_{i,\text{hex}}$	0	-3	3.93	3.66	4.42	4.14	(0.01)
	+1	-2	3.14	2.86	3.02	2.75	(0.01)

well captured by the L^{-3} finite-size scaling. In addition, the potential alignment correction described in Ref. 19 is implicitly taken into account by our extrapolation scheme.²⁵

D. Band gap corrections

The underestimation of the band gap (by the LDA) affects the formation energies, as discussed in detail in the Appendix. A simple correction scheme based on the band energy was proposed by Persson *et al.*²⁶ and is further motivated in the Appendix. The correction amounts to the following term which is added to the as-calculated formation energies:

$$\Delta E^{\text{corr}} = (q + \Delta z_h)\Delta E_{\text{VB}} + \Delta z_e\Delta E_{\text{CB}}, \quad (5)$$

where ΔE_{VB} and ΔE_{CB} are shifts of the valence (VB) and conduction band (CB) edges, respectively, to correct the band gap, while Δz_h and Δz_e are the number of unoccupied valence and occupied conduction band states, respectively.

In the present work, the energy offsets ΔE_{VB} and ΔE_{CB} were obtained from G_0W_0 calculations²⁷ within the single plasmon-pole model as implemented in ABINIT.²⁸⁻³⁰ Non-self-consistent G_0W_0 calculations were employed to properly

refer the quasiparticle energies to the same potential zero as the LDA eigenvalues. Fritz-Haber-Institute norm-conserving pseudopotentials³¹ in the Troullier–Martins scheme³² were used with a cutoff energy of 30 hartree. The other relevant cutoff energies used in the calculation were 5 hartree for the self-energy wave functions, 6 hartree for the exchange part of the self-energy, and 6 hartree for the screening matrix. The number of bands in the self-energy and screening matrix calculations were 100 and 150, respectively.

In Table I, we report both the as-calculated formation energies (including finite-size scaling) and the band-gap-corrected formation energies. The correction terms can be reproduced by using the values for Δz_h and Δz_e included in the table. Note that we extracted Δz_h and Δz_e values only for the most important defects for which an unambiguous distinction between valence and conduction band states was possible. A direct comparison of the as-calculated and band-gap-corrected values is shown in Fig. 3 and is discussed later in Sec. III C.

The defect concentrations calculated in Sec. III D were obtained by using the band-gap-corrected formation energies and the GW band gap.

III. RESULTS

A. Bulk properties

As described in Sec. II A and evident in Eq. (3), the determination of defect formation energies requires that we also calculate bulk properties of the solid and its constituents in reference states. The reference states for Al and Sb are face-centered cubic (fcc) and rhombohedral solids, respectively.

For fcc aluminum, we obtain a lattice constant of 3.99 Å and a cohesive energy of -4.19 eV/atom, which compare reasonably well with the experimental values of 4.05 Å (at room temperature³³) and -3.38 eV/atom.³⁴ The underestimation of the lattice constant and the overestimation of the cohesive energy are typical for LDA calculations. Antimony has a rhombohedral ground-state structure ($R\bar{3}mh$, space group No. 166, *Strukturbericht* symbol A7), for which the DFT calculations yield a lattice constant of 4.46 Å and a rhombohedral angle of 59.0° (experimental values:³³ 4.50 Å and 57.1°) and a cohesive energy of -4.81 eV/atom (experimental value:³⁴ -2.72 eV/atom).

At ambient conditions, bulk aluminum antimonide adopts the zinc-blende structure ($F\bar{4}3m$, space group No. 216, *Strukturbericht* symbol B3). The DFT calculated lattice constant is 6.12 Å, which is in good agreement with the experimental value of 6.13 Å (300 K). The calculated bulk modulus of

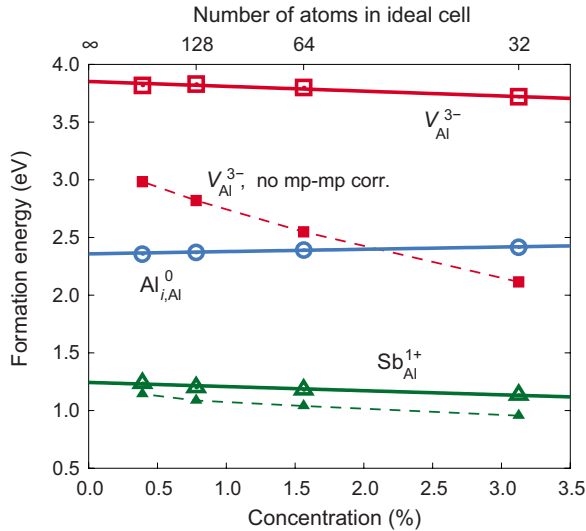


FIG. 1. (Color online) Illustration of finite-size scaling of formation energies to infinite dilution (concentration $\rightarrow 0\%$) for three of the most important defects, with no band gap corrections and $\Delta\mu_e=0$ eV. The small filled and large open symbols respectively show the data without and with the monopole-monopole correction term. Note that, particularly for the charged aluminum vacancy, the monopole-monopole correction is the dominant size-dependent term. The monopole-monopole correction does not apply for neutral defects.

TABLE II. As-calculated formation energies for the split-interstitial configurations that were found to be stable or metastable. Values are given for both Al-rich and Sb-rich conditions. The extrapolation error of the finite-size scaling procedure is given in brackets in the last column. Values are in eV.

Defect	q	Al-rich	Sb-rich	
(Al-Al) _{Al(100)}	-2	6.93	7.20	(0.11)
	-1	5.48	5.76	(0.08)
	0	4.27	4.54	0.06
	+1	3.31	3.58	(0.06)
	+2	3.38	3.65	(0.02)
(Al-Al) _{Al(110)}	-2	4.74	5.02	(0.04)
	-1	3.32	3.60	(0.02)
	0	2.68	2.96	(<0.01)
	+1	2.36	2.64	(0.01)
	+2	2.54	2.82	(0.01)
(Al-Sb) _{Sb(110)}	-2	5.68	5.96	(0.06)
	-1	4.34	4.61	(0.04)
	0	3.34	3.62	(0.01)
	+1	2.68	2.96	(0.01)
	+2	1.68	1.96	(0.01)
(Sb-Al) _{Al(100)}	-2	5.94	5.67	(0.11)
	-1	4.53	4.26	(0.09)
	0	3.91	3.63	(0.03)
(Sb-Al) _{Al(110)}	-2	5.70	5.42	(0.08)
	-1	4.26	3.98	(0.05)
	0	3.46	3.19	(0.01)
	+1	3.01	2.74	(0.07)
	+2	3.00	2.72	(0.01)
(Sb-Sb) _{Sb(100)}	+1	3.72	3.44	(0.02)
	+2	3.72	3.44	(0.01)
(Sb-Sb) _{Sb(110)}	-2	5.13	4.85	(0.11)
	-1	3.72	3.45	(0.08)
	0	3.28	3.00	(0.05)
	+1	3.17	2.90	(0.03)
	+2	3.45	3.18	(0.04)

56 GPa compares well with the experimental value of 59 GPa. The DFT calculations furthermore yield a formation enthalpy of -0.28 eV/f.u. (experimental value: -0.84 eV/f.u.). The direct and indirect band gaps are calculated as 1.53 and 1.12 eV, respectively, while the experimental values are 2.30 and 1.62 eV at 300 K.³⁵ Our calculated values for the lattice constant, bulk modulus, and band gap generally agree with prior DFT results in the literature.^{36–40}

From the *GW* calculations, we obtain direct and indirect band gaps of 2.31 and 1.64 eV, respectively, which are in excellent agreement with the experimental values cited above. The shifts of the valence and conduction band edges showed small variations with the k vector, so we calculated

ΔE_{VB} and ΔE_{CB} , which appear in Eq. (5), as weighted averages over all k points included in the calculations. The shifts thus obtained are $\Delta E_{\text{VB}} = -0.44$ eV and $\Delta E_{\text{CB}} = 0.16$ eV.

B. Defect structures

We considered all possible native defects in AlSb up to split interstitials. In total, this amounts to 18 different defects (two vacancies, two antisite defects, four tetrahedral interstitials, two hexagonal interstitials, and eight split interstitials), not all of which are stable. For each defect, we investigated a series of charge states, generally from $q = -3$ to $q = +3$, as appropriate. Defect complexes were not considered.

Vacancies. In the ideal zinc-blende structure, both Al and Sb sites possess tetrahedral symmetry with nearest neighbor distance of 2.65 Å. If one removes a single atom and allows the system to relax from randomized positions, the aluminum vacancy V_{Al} maintains the T_d symmetry for all relevant charge states and the surrounding antimony ions relax inward from 0.36 Å (for $q=0$) to 0.38 Å (for $q=-3$) [see, for example, Fig. 2(a)]. This behavior is typical of cation vacancies in III-V and II-VI zinc-blende semiconductors, where a dimerization transformation of the atoms surrounding the vacancy is generally not energetically favorable.⁴¹ In contrast, the antimony vacancy V_{Sb} exhibits a Jahn–Teller distortion to a local tetragonal symmetry for all but the positive charge states. The relaxed configuration for V_{Sb}^{3+} is shown in Fig. 2(b) representatively, which also indicates the pairing of Al atoms in the first neighbor shell of the vacancy.

Antisites. Both Al_{Sb} and Sb_{Al} antisite defects maintain the T_d symmetry for all relevant charge states. In the case of Al_{Sb} , the surrounding aluminum ions relax inward, while for Sb_{Al} , the nearest neighbor antimony ions relax outward [cf. Figs. 2(c) and 2(d)]. These relaxations occur as expected based on the atomic radii.

Tetrahedral interstitials. In the zinc-blende structure, there are two distinct tetrahedral sites: one centered on an Al tetrahedron ($4d$ site) and one centered on an Sb tetrahedron ($4b$ site). Thus, there are four possible types of tetrahedral interstitials: $\text{Al}_{i,\text{Al}}$ and $\text{Sb}_{i,\text{Al}}$ on the $4d$ site; $\text{Al}_{i,\text{Sb}}$ and $\text{Sb}_{i,\text{Sb}}$ on the $4b$ site.

Both kinds of tetrahedral aluminum interstitials ($\text{Al}_{i,\text{Al}}$, $\text{Al}_{i,\text{Sb}}$) maintain the T_d symmetry after relaxation, with the neighboring ions relaxing outward as shown in Figs. 2(f) and 2(g). The $\text{Sb}_{i,\text{Sb}}$ configuration is unstable in all but the +2 charge state; in all other charge states, the interstitial atom relaxes either onto a hexagonal site or forms a split interstitial. Conversely, $\text{Sb}_{i,\text{Al}}$ is stable in all of its charge states, but does exhibit Jahn–Teller distortions as illustrated in Fig. 2(h).

Hexagonal interstitials. The hexagonal interstitial is located at Wyckoff position 16e. The aluminum hexagonal interstitial $\text{Al}_{i,\text{hex}}$ was found to be unstable for all charge states, with the Al atom observed to relax into the $\text{Al}_{i,\text{Al}}$ configuration even when starting from ideal positions. For the antimony hexagonal interstitial $\text{Sb}_{i,\text{hex}}$, the +2 charge state was found to relax directly into the $\text{Sb}_{i,\text{Al}}$ position, whereas for charge states +1 and -2, the interstitial atom remained in the hexagonal site. The other charge states when perturbed from

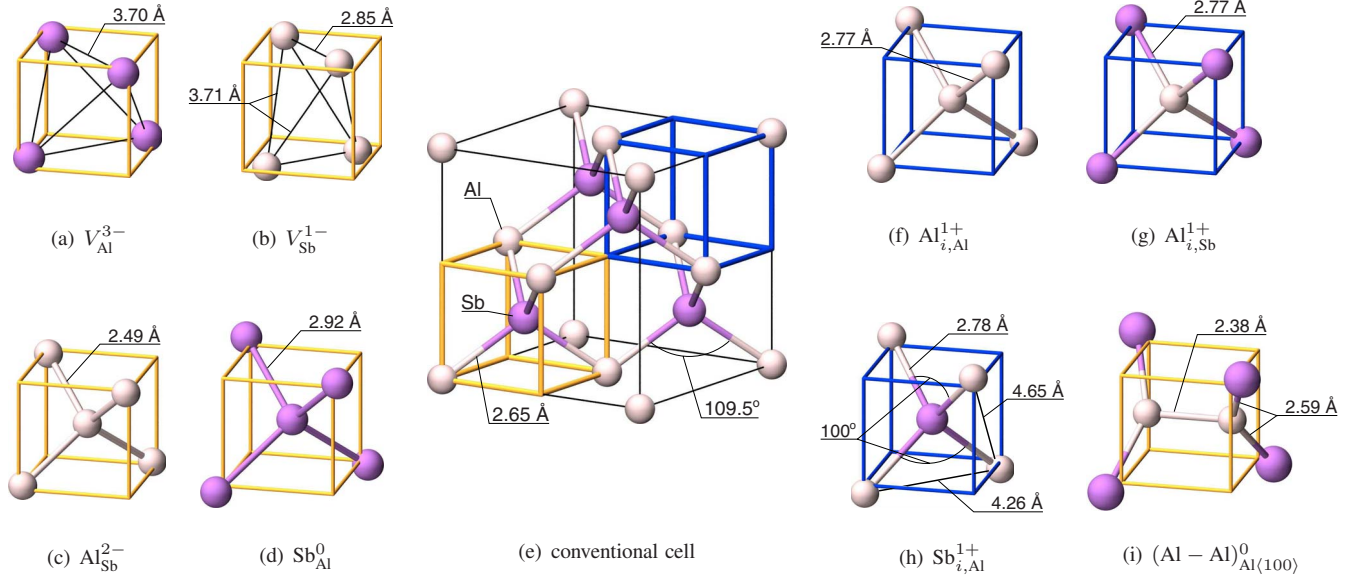


FIG. 2. (Color online) Relaxed defect geometries for [(a) and (b)] vacancies, [(c) and (d)] antisites, [(f)–(h)] several tetrahedral interstitials, and (i) one split interstitial. (e) The conventional 8-atom unit cell is shown for reference. Purple (dark gray) and beige (light gray) balls represent antimony and aluminum atoms, respectively. Note that the negatively charged antimony vacancy in (b) shows a pronounced Jahn–Teller distortion. (Indicated bond lengths were taken from 216-atom supercells.)

the ideal position relax into the $(\text{Sb-Sb})_{\text{Sb}\langle 110 \rangle}$ split interstitial, described below.

Split interstitials. Split interstitial configurations, in which two atoms share one atom site, have been extensively discussed in the literature for the zinc-blende structure.^{11,42–47} We have carried out an exhaustive exploration of the structures of these defects in AlSb. The following cases were considered: two Al atoms oriented along $\langle 100 \rangle$ sharing one Al site $[(\text{Al-Al})_{\text{Al}\langle 100 \rangle}]$, the same atoms but oriented along $\langle 110 \rangle$ $[(\text{Al-Al})_{\text{Al}\langle 110 \rangle}]$, one Al atom and one Sb atom oriented along $\langle 100 \rangle$ sharing one Al site $[(\text{Sb-Al})_{\text{Al}\langle 100 \rangle}]$, and the same combination of atoms oriented along $\langle 110 \rangle$ $[(\text{Sb-Al})_{\text{Al}\langle 110 \rangle}]$. Four more configurations are obtained, which correspond to the same combinations above but sharing an Sb site.

Most of these configurations are actually found to be unstable with respect to other interstitial configurations. The results of these calculations are summarized in Table III,

which shows which configurations were found to be stable and which ones were unstable or only conditionally stable with respect to alternative interstitial configurations. In certain cases, a structure relaxed starting from the ideal atomic coordinates maintained the starting symmetry after relaxation, but when started from randomized coordinates, the structure relaxed to a different configuration; these cases are indicated in Table III with a superscript “a” and listing the lower energy relaxed structure. The cases simply marked “Stable” in Table III relaxed to the ideal symmetry configuration for all starting configurations.

For completeness, we note that the split interstitial $(\text{Sb-Al})_{\text{Al}\langle 100 \rangle}$ in charge states $q=0, -1$, and -2 is displaced along $\langle 100 \rangle$ from the ideal position, such that the Sb interstitial is located in between two regular Sb atoms along the $\langle 110 \rangle$ direction. These structures are indicated in Table III with a superscript “b”.

TABLE III. Stability of split-interstitial configurations.

Charge state	+2	+1	0	-1	-2
$(\text{Al-Al})_{\text{Al}\langle 100 \rangle}$	$\text{Al}_{i,\text{Sb}}^{\text{a}}$	Stable	$\text{Al}_{i,\text{Al}}^{\text{a}}$	$(\text{Al-Al})_{\text{Al}\langle 110 \rangle}^{\text{a}}$	$(\text{Al-Al})_{\text{Al}\langle 110 \rangle}^{\text{a}}$
$(\text{Al-Al})_{\text{Al}\langle 110 \rangle}$	$\text{Al}_{i,\text{Al}}^{\text{a}}$	$\text{Al}_{i,\text{Al}}^{\text{a}}$	Stable	Stable	Stable
$(\text{Al-Sb})_{\text{Sb}\langle 100 \rangle}$	$\text{Al}_{i,\text{Al}}$	$\text{Al}_{i,\text{Al}}$	$\text{Al}_{i,\text{Al}}$	$\text{Al}_{i,\text{Al}}$	$\text{Al}_{i,\text{Al}}$
$(\text{Al-Sb})_{\text{Sb}\langle 110 \rangle}$	$\text{Al}_{i,\text{Al}}$	Stable	Stable	Stable	Stable
$(\text{Sb-Sb})_{\text{Sb}\langle 100 \rangle}$	$\text{Sb}_{i,\text{Al}}^{\text{a}}$	$\text{Sb}_{i,\text{Al}}^{\text{a}}$	$(\text{Sb-Sb})_{\text{Sb}\langle 110 \rangle}$	$(\text{Sb-Sb})_{\text{Sb}\langle 110 \rangle}$	$(\text{Sb-Sb})_{\text{Sb}\langle 110 \rangle}$
$(\text{Sb-Sb})_{\text{Sb}\langle 110 \rangle}$	Stable	Stable	Stable	Stable	Stable
$(\text{Sb-Al})_{\text{Al}\langle 100 \rangle}$	$(\text{Sb-Sb})_{\text{Sb}\langle 110 \rangle}$	$(\text{Sb-Sb})_{\text{Sb}\langle 110 \rangle}$	Stable ^b	Stable ^b	Stable ^b
$(\text{Sb-Al})_{\text{Al}\langle 110 \rangle}$	Stable	Stable	Stable	Stable	Stable

^aRelaxations starting from the idealized positions maintained the initial symmetry, but when started from randomized positions, relaxed to the indicated structure.

^bSplit interstitial displaced along $\langle 100 \rangle$ from ideal position.

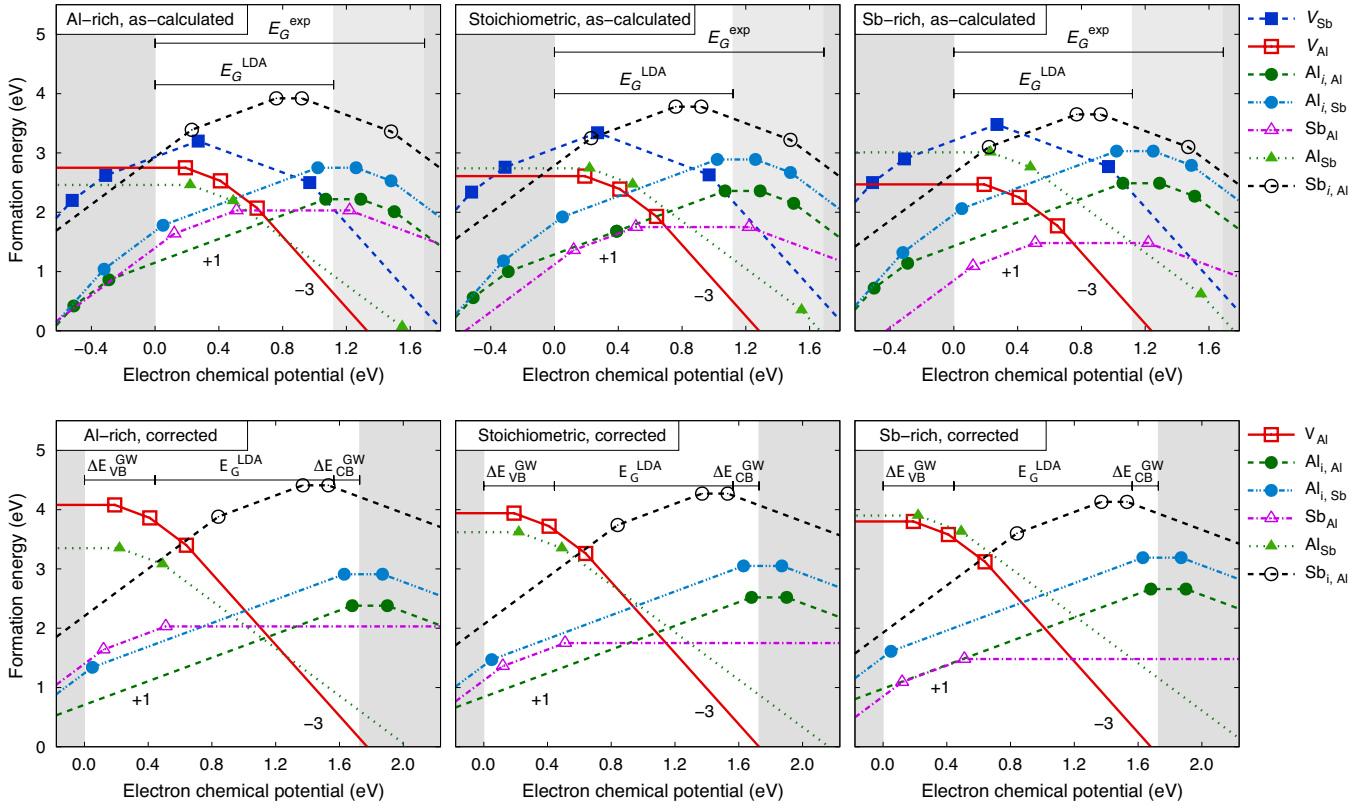


FIG. 3. (Color online) Dependence of the formation energies on the electron chemical potential under Al-rich (left, $\Delta\mu = -\Delta H_f$), stoichiometric (center, $\Delta\mu = 0$ eV), and Sb-rich (right, $\Delta\mu = +\Delta H_f$) conditions for the most important point defects. The top panels show the formation energies based on the as-calculated values, while the bottom panels show the results of applying the band gap correction term of Eq. (5). The slope of each line is determined by the charge state, according to Eq. (3) ($\Delta H_f^{\text{calc}} = -0.28$ eV).

C. Formation energies

The defect formation energies calculated by using Eq. (3) for Al-rich and Sb-rich conditions and an electron chemical potential at the valence band maximum are given in Tables I and II. The formation energies for the dominant defects (lowest ΔE_D) are shown as a function of the electron chemical potential in Fig. 3.

Figure 3 also illustrates the effect of the band gap correction described in Sec. II D. In the top row, we show the formation energies after the finite-size scaling procedure was applied, but without the band gap correction. The bottom row shows the results including the band gap corrections. It is apparent that as the band gap correction is applied, donor and acceptor levels track the conduction and valence band edges, respectively. This feature is independent of the relative values of $\Delta E_{\text{VB}}^{\text{GW}}$ and $\Delta E_{\text{CB}}^{\text{GW}}$ in Eq. (5).

It is interesting to compare the band-gap-corrected formation energies in the bottom panel of Fig. 3 with those in the top panel if the band gap is simply extended to the experimental value by shifting the conduction band upward. Considerable differences are observed between the two cases, with the values corrected by using the scheme presented here being more consistent. In fact, we observe that, qualitatively, the results obtained by applying no correction at all are more similar to the corrected results than what is obtained by assigning the band gap error fully to the conduction band.^{48,49} Furthermore, a correction procedure often suggested in

literature⁴⁵ to simply shift the ionization energies of donor-like defects to track the conduction band minimum (implicitly leaving the ionization energies of acceptorlike defects tracking the valence band maximum), without accounting for the occupation of states, does not properly correct the errors in the formation energies. The scheme employed here results in an identical shift of the ionization energies, but also corrects the errors in the formation energies. However, we note that this scheme still neglects both level relaxations and changes in the double counting term.

We believe that the method presented here is the most consistent way to address the LDA band gap problem. Our use of *GW* calculations provides a first principles approach to calculating the correction terms. We find that neglecting to include the band gap correction terms in the formation energies leads to significant errors in the prediction of defect concentrations and of which defects are dominant.

D. Defect and charge carrier concentrations

With the formation energies known, the equilibrium defect concentrations for a given chemical potential difference $\Delta\mu$ can be calculated by using Eq. (1). The defect concentrations depend on the electron chemical potential via Eq. (3). In the absence of extrinsic defects, the electron chemical potential is constrained by the charge neutrality condition

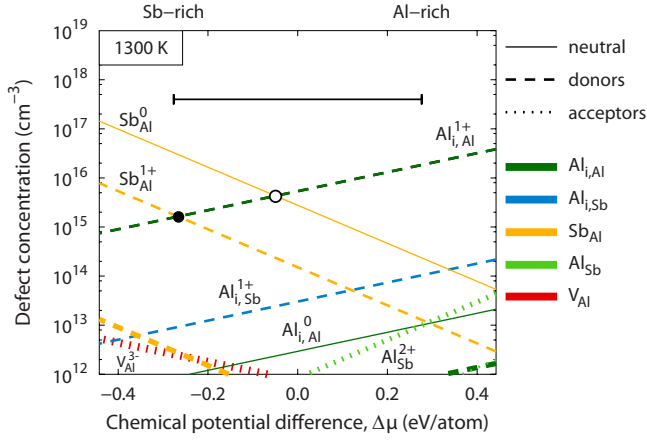


FIG. 4. (Color online) Concentrations of individual defects at a temperature of 1300 K as a function of the chemical potential difference $\Delta\mu$. Line thicknesses scale with charge state. Under Sb-rich conditions, the dominant defect is the neutral Sb_{Al}^0 antisite, whereas under Al-rich conditions, the positively charged aluminum interstitial $\text{Al}_{\text{i,Al}}^{1+}$ is dominant. The crossover point between $\text{Al}_{\text{i,Al}}^{1+}$ and Sb_{Al}^0 (open circle) determines the minimum in the total defect concentration shown in Fig. 5(a), while the crossover point between $\text{Al}_{\text{i,Al}}^{1+}$ and $\text{Sb}_{\text{Al}}^{1+}$ (filled circle) determines the minimum in the net electron concentration shown in Fig. 5(b). The horizontal bar marks the calculated range of variation of $\Delta\mu$ given by the formation enthalpy of the compound ($-\Delta H_f \leq \Delta\mu \leq +\Delta H_f$, with $\Delta H_f^{\text{calc}} = -0.28$ eV).

$$0 = n_e - n_h - \sum_i^{\text{defects}} q_i c_i, \quad (6)$$

since the intrinsic concentrations of electrons and holes, n_e and n_h , respectively, are given by

$$n_e = \int D(E) f(E; \mu_e) dE, \quad (7a)$$

$$n_h = \int D(E) [1 - f(E; \mu_e)] dE. \quad (7b)$$

Here, $D(E)$ is the electronic density of states and $f(E; \mu_e) = \{1 + e^{(E - \mu_e)/k_B T}\}^{-1}$ is the Fermi-Dirac distribution. The implicit dependence of the charge neutrality condition on the electron chemical potential μ_e is apparent from Eqs. (7a) and (7b). To obtain the charge carrier and defect concentrations, then, we must iteratively solve Eq. (6) to self-consistently determine the intrinsic electron chemical potential.

The defect concentrations calculated by using the band-gap-corrected formation energies are shown in Fig. 4 for a representative temperature of 1300 K ($T_{\text{melt}}^{\text{AlSb}} = 1327$ K), with the line thicknesses indicating the charge state $|q|$. Figure 5 shows the dependence of the total defect and net electron concentrations on the chemical environment (chemical potential difference $\Delta\mu$) for a variety of temperatures. For all cases shown here, the intrinsic (self-consistent) electron chemical potential is located near the middle of the gap, although there are slightly more electrons than holes in the material (intrinsically n -type material).

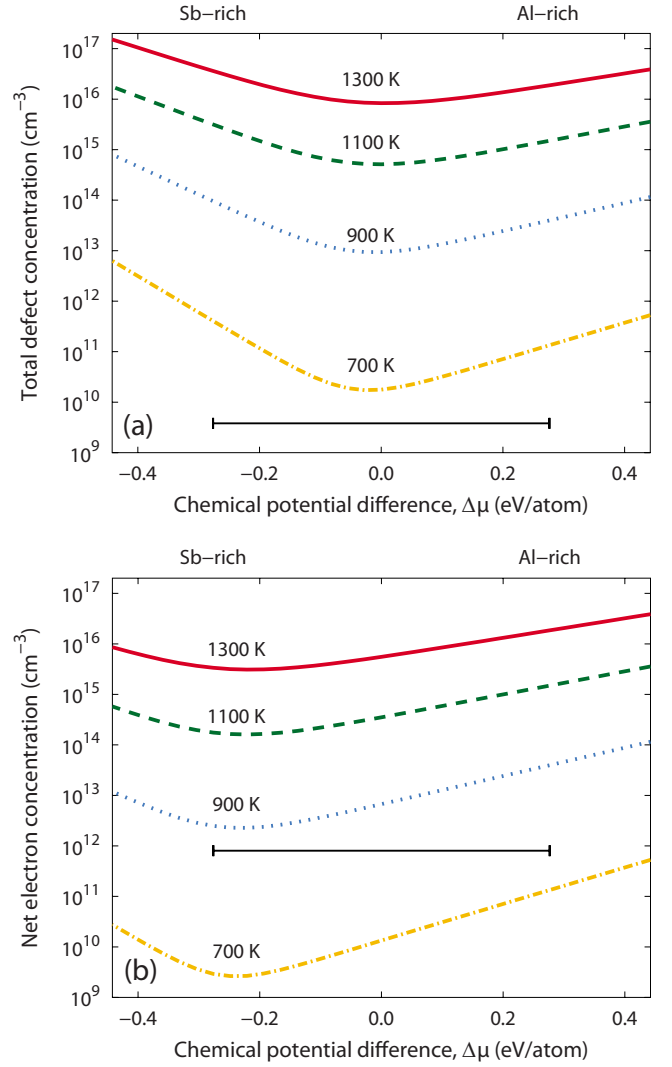


FIG. 5. (Color online) (a) Equilibrium total defect concentration and (b) net electron concentration ($n_e - n_h$) at different temperatures as a function of the chemical potential difference. Note that the minimum in the total defect concentration corresponds to the crossover point between $\text{Al}_{\text{i,Al}}^{1+}$ and Sb_{Al}^0 , while the minimum in the net electron concentration corresponds to the crossover point between $\text{Al}_{\text{i,Al}}^{1+}$ and $\text{Sb}_{\text{Al}}^{1+}$, as indicated in Fig. 4. The dominant defects on the Sb-rich side are Sb_{Al} and on the Al-rich side are $\text{Al}_{\text{i,Al}}$. The horizontal bar marks the calculated range of variation of $\Delta\mu$ given by the formation enthalpy of the compound ($-\Delta H_f \leq \Delta\mu \leq +\Delta H_f$, with $\Delta H_f^{\text{calc}} = -0.28$ eV).

IV. DISCUSSION

An inspection of the G_0W_0 -corrected results in the lower panels of Fig. 3 shows that four different defects have the lowest formation energy and are thus the most abundant, depending on the values of the electron chemical potential μ_e and the chemical potential difference $\Delta\mu$. The aluminum tetrahedral interstitial $\text{Al}_{\text{i,Al}}^{1+}$ is the dominant defect for μ_e in the lower half of the band gap (p -type material), while the aluminum vacancy V_{Al}^{3-} is dominant for μ_e in the upper half of the band gap (n -type material). For Al-rich conditions (left panel in Fig. 3), the $\text{Al}_{\text{Sb}}^{2-}$ antisite defect can also be important

when the material is lightly doped n -type (near the crossing with V_{Al}^{3-}), particularly considering the uncertainty in the range of $\Delta\mu^{\text{calc}}$ vs $\Delta\mu^{\text{expt}}$ and the possible errors in the formation energies of up to ~ 0.1 eV from entropic effects. For Sb-rich conditions (right panel in Fig. 3), the Sb_{Al} antisite defect (neutral or positively charged) is important over a wide range of μ_e , from the p -type regime to near the middle of the gap. However, we note that for μ_e near the middle of the gap (intrinsic or compensated material), the dominant charged native defect is always $\text{Al}_{i,\text{Al}}^{1+}$, since the relevant Sb_{Al}^0 defect is uncharged.

In the absence of impurities, the intrinsic electron chemical potential is located near the middle of the band gap (see Sec. III D). Under this condition, the two relevant defects are therefore the $\text{Al}_{i,\text{Al}}^{1+}$ interstitial and the Sb_{Al} antisite, as illustrated clearly in Fig. 4. By comparison with Fig. 5(a), we see that the transition point between $\text{Al}_{i,\text{Al}}^{1+}$ and Sb_{Al}^0 , which occurs close to $\Delta\mu=0$ eV, corresponds to the minimum in the total defect concentration. In Fig. 5(a), the dominant defect on the Sb-rich (left) side is Sb_{Al}^0 , while on the Al-rich (right) side it is $\text{Al}_{i,\text{Al}}^{1+}$. Near the transition (minimum in the curve), the two concentrations are comparable. In contrast, the minimum in the net electron concentration in Fig. 5(b) is located on the Sb-rich side, which corresponds to the crossing of the concentrations of $\text{Al}_{i,\text{Al}}^{1+}$ and Sb_{Al}^0 in Fig. 4. Since the charge neutrality condition [Eq. (6)] depends only on the concentrations of charged defects, the neutral Sb_{Al}^0 antisites do not contribute to charge compensation or net electron concentration.

As mentioned in Sec. III D, the calculated electron concentration slightly exceeds the hole concentration for pure material, which yields n -type intrinsic material irrespective of the chemical environment characterized by $\Delta\mu$. This behavior results because the formation energies of acceptor-type defects (V_{Al}^{3-}) always exceed the formation energies of donor-type defects ($\text{Al}_{i,\text{Al}}^{1+}$, $\text{Sb}_{\text{Al}}^{1+}$) when the electron chemical potential is close to the middle of the band gap (see Fig. 3). It should be noted that this situation can change if the material is extrinsically doped. For a p -doped material, the donor-type native defects remain dominant and partially compensate the extrinsic dopant. For a n -doped material, the ordering of the formation energies is reversed, but the then-dominant acceptor-type native defects still partially compensate the extrinsic dopant.

The temperatures indicated in Figs. 4 and 5 refer to thermal equilibrium conditions at those temperatures. In practice, these temperatures can be interpreted as corresponding to annealing temperatures, with the chemical potential difference referring to the chemical environment of the annealing process (e.g., an Sb overpressure corresponds to Sb-rich conditions; conversely, growth is often performed under Al-rich conditions). The highest temperature considered here, 1300 K, is just below the melting point of 1327 K and might represent melt growth conditions. However, growth is typically performed too rapidly to allow equilibrium to be achieved and the nonequilibrium grown-in defect concentrations will be higher than predicted here. The curves in Fig. 5 essentially represent the predicted concentrations for infinitely long anneals at the specified temperatures.

At 1300 K, the calculated net electron concentration varies roughly between 10^{16} and 10^{17} cm^{-3} depending on the

chemical potential difference, $\Delta\mu$. If all defects are assumed to be sufficiently mobile down to 700 K so that the material can reach thermal equilibrium at that temperature, then the lowermost curves in Fig. 5 predict a net electron concentration of 10^{10} – 10^{11} cm^{-3} and a total defect concentration between 10^{10} and 10^{12} cm^{-3} . Since the diffusivity exponentially depends on the inverse temperature, the defect mobilities sharply decrease with temperature. Therefore, as the temperature is further lowered, the system will no longer be able to reach the equilibrium concentration in reasonable time, which requires excess defects either to diffuse to the surface or to anneal by recombination. In contrast to lattice defects, the intrinsic electron and hole concentrations, n_e and n_h , readily adjust to temperature changes. The freezing in of the defect concentrations is therefore expected to crucially affect the charge neutrality condition upon cooling to low (e.g., room) temperatures (in particular, if there are no extrinsic dopants). However, since the diffusivities of the individual defects are currently unknown, we cannot quantitatively describe this freezing in of the defect distributions in the present study; thus, predictions of the charge carrier and defect concentrations near room temperature and below may be unreliable. The determination of diffusivities for specific defects, to account for the kinetics of defects freezing in, will be the subject of future work.

Experimentally, AlSb crystals grown from the melt have often been found to display p -type conductivity.⁵⁰ The present finding that the pure material behaves intrinsically n type is, however, not in contradiction with this observation. A typical experimental setup employs a graphite susceptor and an alumina crucible, with quartz tubes used for melting Sb, all which are potential sources of various impurities, most importantly carbon, oxygen, silicon, and aluminum.⁵⁰ In particular, carbon impurities act as acceptors, so unintentional p -type doping is very likely, which is supported by a chemical analysis of grown AlSb crystals and measurements on intentionally doped samples.⁵⁰ The measured levels of carbon impurities and the experimental observation that the material becomes intrinsic at around 1000 K (Ref. 35) are consistent with our calculated excess native electron concentration at that temperature. A detailed study of the role of extrinsic defects in AlSb is beyond the scope of the present work: however, the results of ongoing work to elucidate the effects of impurities and to investigate ways to optimize the electronic properties of the material by intentional doping are forthcoming.

V. CONCLUSIONS

In summary, we have employed density functional theory calculations to study the properties of intrinsic point defects in aluminum antimonide. An exhaustive set of defect configurations—including vacancies, antisites, and interstitials (tetrahedral, hexagonal, and split), with all relevant charge states—was considered based on knowledge of other III-V compounds. Relaxed atomic structures of each defect were carefully determined, and formation energies were calculated to evaluate the equilibrium concentrations of each defect. Strain and electrostatic artifacts related to the use of

the supercell approach were carefully removed by employing a finite-size scaling procedure, which involved performing a series of calculations for each defect with supercell sizes ranging from 32 to 216 atoms. The underestimation of the band gap due to the local density approximation was taken into account by applying an *a posteriori* correction scheme that utilized separate *GW* calculations to obtain valence and conduction band offsets, which enter the correction.

Aluminum interstitials ($\text{Al}_{i,\text{Al}}^{1+}$), antimony antisites (Sb_{Al}^0 , $\text{Sb}_{\text{Al}}^{1+}$), and aluminum vacancies ($\text{V}_{\text{Al}}^{3-}$) were found to be the most dominant defects, depending on the electron chemical potential and the chemical potential difference (chemical environment) of the system. We observe that $\text{Al}_{i,\text{Al}}^{1+}$ interstitials and Sb_{Al} antisites dominate under Al-rich and Sb-rich conditions, respectively. Calculated formation energies were employed in solving the charge neutrality condition to obtain self-consistent defect concentrations and intrinsic electron chemical potential for the pure material at various temperatures. We find the material to be intrinsically weakly *n* type and predict both the total defect and the net electron concentrations. Near the melting point, the equilibrium concentration of native defects is predicted to be in the 10^{16} – 10^{17} cm^{-3} range, while at lower temperatures, it is expected that concentrations down to the 10^{10} cm^{-3} range or lower can be achieved. The net excess electron density in a bulk grown material might be as high as 10^9 – 10^{11} cm^{-3} due to defects freezing in during melt solidification.

For an extrinsically doped material, which we do not treat explicitly in detail in this work, the dominant native defects depend on the nature of the doping. For *n*-doped material, $\text{V}_{\text{Al}}^{3-}$ and $\text{Al}_{\text{Sb}}^{2-}$ tend to be important, while for *p*-doped material, $\text{Al}_{i,\text{Al}}^{1+}$ and $\text{Sb}_{\text{Al}}^{1+}$ are important, depending on chemical environment (Al-rich vs Sb-rich). Some amount of self-compensation from the native defects occurs in both cases.

Finally, we note that the present work is part of a concerted research effort, which ultimately aims to provide a complete and consistent picture of the point defect properties of AlSb and the relations to carrier transport properties. We are engaged in further theoretical and experimental work to explore the role of extrinsic defects, as well as the scattering behavior of defects on carrier transport. In this context, the present study forms the basis for these future studies, which will be the subjects of forthcoming reports.

ACKNOWLEDGMENTS

This work was performed under the auspices of the U.S. Department of Energy by Lawrence Livermore National Laboratory in part under Contract No. W-7405-Eng-48 and in part under Contract No. DE-AC52-07NA27344. The authors acknowledge support from the National Nuclear Security Administration Office of Nonproliferation Research and Development (NA-22) and from the Laboratory Directed Research and Development Program at LLNL. The authors would like to thank Babak Sadigh for fruitful discussions.

APPENDIX: BAND GAP CORRECTION OF DEFECT FORMATION ENERGIES

While DFT calculations typically give very reasonable values for energy differences *within* a group of bands (e.g.,

the valence band), energy differences *between* different groups of bands (i.e., band gaps, e.g., between the valence and conduction bands) are much less reliable. This shortcoming particularly affects the differences between the valence and conduction bands, which gives rise to the well-known band gap error.

The incorrect description of the energy differences between different groups of bands can affect the total energy. The most sensitive contribution is the band energy which is given by

$$E_b = \sum_i \sum_k f_{ik} \varepsilon_{ik}, \quad (\text{A1})$$

where *i* and *k* run over bands and *k* points, respectively, and f_{ik} and ε_{ik} are the occupation numbers and eigenvalues, respectively. Without loss of generality, one can divide the band energy into separate sums over the valence and conduction band states, as

$$E_b = \sum_i^{\text{VB}} \sum_k f_{ik} \varepsilon_{ik} + \sum_i^{\text{CB}} \sum_k f_{ik} \varepsilon_{ik}. \quad (\text{A2})$$

If one assumes rigid levels, which is a reasonable approximation in many cases, the errors in the energy differences between two groups of bands (i.e., across a band gap) can be corrected by adding constant energy shifts to the valence and conduction band states:

$$\varepsilon_{ik} \rightarrow \varepsilon_{ik} + \Delta E_{\text{VB}} \quad \text{for the valence band,}$$

$$\varepsilon_{ik} \rightarrow \varepsilon_{ik} + \Delta E_{\text{CB}} \quad \text{for the conduction band.}$$

The sum of the band shifts, $\Delta E_{\text{VB}} + \Delta E_{\text{CB}}$, equals the band gap error. The expression for the corrected band energy then reads

$$\tilde{E}_b = \sum_i^{\text{VB}} \sum_k f_{ik} (\varepsilon_{ik} + \Delta E_{\text{VB}}) + \sum_i^{\text{CB}} \sum_k f_{ik} (\varepsilon_{ik} + \Delta E_{\text{CB}}). \quad (\text{A3})$$

By taking the difference between Eqs. (A2) and (A3), one obtains the band energy correction term

$$\begin{aligned} \Delta E_b^{\text{corr}} &= (\tilde{E}_b - E_b)_{\text{defect}} - (\tilde{E}_b - E_b)_{\text{ideal}} \\ &= \Delta E_{\text{VB}} \underbrace{\sum_i^{\text{VB}} \sum_k (f_{ik} - 1)}_{\Delta z_h} + \Delta E_{\text{CB}} \underbrace{\sum_i^{\text{CB}} \sum_k f_{ik}}_{\Delta z_e}, \end{aligned} \quad (\text{A4})$$

where Δz_h is simply the number of unoccupied states in the valence band and Δz_e is the number of occupied states in the conduction band.

According to Eq. (3), the defect formation energy of charged defects further depends on the position of the

valence band maximum. The total correction term for the formation energy thus reads

$$\Delta E^{corr} = (q + \Delta z_h)\Delta E_{VB} + \Delta z_e\Delta E_{CB}. \quad (\text{A5})$$

The energy offsets ΔE_{VB} and ΔE_{CB} can be obtained, for example, from *GW* calculations, which for many systems provide band gaps and structures in good agreement with experiment.

It is important to realize that this scheme neglects both level relaxations and changes in the double counting term. If these limitations are acceptable, this method offers a simple *a posteriori* correction of the formation energies. It should furthermore be noted that transition levels are not affected by the relative weight of ΔE_{VB} and ΔE_{CB} . Upon application of this correction scheme, acceptor levels track the valence band maximum while donor transitions follow the conduction band minimum.

*aberg2@llnl.gov

†lordi2@llnl.gov

- ¹G. A. Armantrout, S. P. Swierkowski, J. W. Sherohman, and J. H. Lee, *IEEE Trans. Nucl. Sci.* **N5–24**, 121 (1977).
- ²A. Owens, *J. Synchrotron Radiat.* **13**, 143 (2006).
- ³G. Tuttle and H. Kroemer, *IEEE Trans. Electron Devices* **ED-34**, 2358 (1987).
- ⁴T. Ashley *et al.*, *Electron. Lett.* **43**, 777 (2007).
- ⁵R. Soderstrom, E. R. Brown, C. D. Parker, L. J. Mahoney, and T. C. McGill, *Appl. Phys. Lett.* **58**, 275 (1991).
- ⁶C. L. Canedy, W. W. Bewley, J. R. Lindle, C. S. Kim, M. Kim, I. Vurgaftman, and J. R. Meyer, *Appl. Phys. Lett.* **88**, 161103 (2006).
- ⁷C. L. Canedy, W. W. Bewley, M. Kim, C. S. Kim, J. A. Nolde, D. C. Larrabee, J. R. Lindle, I. Vurgaftman, and J. R. Meyer, *Appl. Phys. Lett.* **90**, 181120 (2007).
- ⁸J. Devenson, R. Teissier, O. Cathabard, and A. N. Baranov, *Appl. Phys. Lett.* **90**, 111118 (2007).
- ⁹A. R. Allnatt and A. B. Lidiard, *Atomic Transport in Solids* (Cambridge University Press, Cambridge, 2003).
- ¹⁰G.-X. Qian, R. M. Martin, and D. J. Chadi, *Phys. Rev. B* **38**, 7649 (1988).
- ¹¹S. B. Zhang and J. E. Northrup, *Phys. Rev. Lett.* **67**, 2339 (1991).
- ¹²G. Kresse and J. Hafner, *Phys. Rev. B* **47**, 558 (1993).
- ¹³G. Kresse and J. Hafner, *Phys. Rev. B* **49**, 14251 (1994).
- ¹⁴G. Kresse and J. Furthmüller, *Phys. Rev. B* **54**, 11169 (1996).
- ¹⁵G. Kresse and J. Furthmüller, *Comput. Mater. Sci.* **6**, 15 (1996).
- ¹⁶P. E. Blöchl, *Phys. Rev. B* **50**, 17953 (1994).
- ¹⁷G. Kresse and D. Joubert, *Phys. Rev. B* **59**, 1758 (1999).
- ¹⁸H. J. Monkhorst and J. D. Pack, *Phys. Rev. B* **13**, 5188 (1976).
- ¹⁹Y.-J. Zhao, C. Persson, S. Lany, and A. Zunger, *Appl. Phys. Lett.* **85**, 5860 (2004).
- ²⁰P. Erhart, K. Albe, and A. Klein, *Phys. Rev. B* **73**, 205203 (2006).
- ²¹D. Grecu and P. H. Dederichs, *Phys. Lett.* **36A**, 135 (1971).
- ²²P. H. Dederichs and J. Pollmann, *Z. Phys.* **255**, 315 (1972).
- ²³G. Makov and M. C. Payne, *Phys. Rev. B* **51**, 4014 (1995).
- ²⁴J. Lento, J.-L. Mozos, and R. M. Nieminen, *J. Phys.: Condens. Matter* **14**, 2637 (2002).
- ²⁵P. Erhart and K. Albe, *J. Appl. Phys.* **102**, 084111 (2007).
- ²⁶C. Persson, Y.-J. Zhao, S. Lany, and A. Zunger, *Phys. Rev. B* **72**, 035211 (2005).
- ²⁷L. Hedin, *Phys. Rev.* **139A**, 796 (1965).
- ²⁸X. Gonze *et al.*, *Comput. Mater. Sci.* **25**, 478 (2002).
- ²⁹S. Goedecker, *SIAM J. Sci. Comput. (USA)* **18**, 1605 (1997).
- ³⁰The ABINIT code is a common project of the Université Catholique de Louvain, Corning Incorporated, and other contributors (<http://www.abinit.org>).
- ³¹M. Fuchs and M. Scheffler, *Comput. Phys. Commun.* **119**, 67 (1999).
- ³²N. Troullier and J. L. Martins, *Phys. Rev. B* **43**, 1993 (1991).
- ³³*Binary Alloy Phase Diagrams*, edited by T. B. Massalski (ASM International, Metals Park, OH, 1986).
- ³⁴A. M. James and M. P. Lord, *Macmillan's Chemical and Physical Data* (Macmillan, London, 1992).
- ³⁵O. Madelung, *Semiconductors: Data Handbook*, 3rd ed. (Springer, New York, 2004).
- ³⁶M. Puska, *J. Phys.: Condens. Matter* **1**, 7347 (1989).
- ³⁷P. Giannozzi, S. de Gironcoli, P. Pavone, and S. Baroni, *Phys. Rev. B* **43**, 7231 (1991).
- ³⁸X. Zhu and S. G. Louie, *Phys. Rev. B* **43**, 14142 (1991).
- ³⁹S. Q. Wang and H. Q. Ye, *Phys. Rev. B* **66**, 235111 (2002).
- ⁴⁰W. Liu, W. T. Zheng, and Q. Jiang, *Phys. Rev. B* **75**, 235322 (2007).
- ⁴¹D. J. Chadi, *Mater. Sci. Semicond. Process.* **6**, 281 (2003).
- ⁴²G. A. Baraff and M. Schlüter, *Phys. Rev. Lett.* **55**, 1327 (1985).
- ⁴³D. J. Chadi, *Phys. Rev. B* **46**, 9400 (1992).
- ⁴⁴K. Laasonen, R. M. Nieminen, and M. J. Puska, *Phys. Rev. B* **45**, 4122 (1992).
- ⁴⁵J. T. Schick, C. G. Morgan, and P. Papoulias, *Phys. Rev. B* **66**, 195302 (2002).
- ⁴⁶G. Zollo and R. M. Nieminen, *J. Phys.: Condens. Matter* **15**, 843 (2003).
- ⁴⁷F. El-Mellouhi and N. Mousseau, *Phys. Rev. B* **71**, 125207 (2005).
- ⁴⁸A. S. Foster, V. B. Sulimov, F. Lopez Gejo, A. L. Shluger, and R. M. Nieminen, *Phys. Rev. B* **64**, 224108 (2001).
- ⁴⁹A. F. Kohan, G. Ceder, D. Morgan, and Chris G. Van de Walle, *Phys. Rev. B* **61**, 15019 (2000).
- ⁵⁰K. J. Wu (private communication).